Monthly Notices of the ROYAL ASTRONOMICAL SOCIETY

MNRAS **465,** 3220–3234 (2017)
Advance Access publication 2016 November 4

doi:10.1093/mnras/stw2827

# The COSMOS-[O II] survey: evolution of electron density with star formation rate

Melanie Kaasinen,★ Fuyan Bian,★† Brent Groves, Lisa J. Kewley and Anshu Gupta

*Research School of Astronomy and Astrophysics, Australian National University, Weston Creek 2611, Australia*

Accepted 2016 November 1. Received 2016 October 12; in original form 2016 August 16

## ABSTRACT

Star-forming galaxies at $z > 1$ exhibit significantly different properties to local galaxies of equivalent stellar mass. Not only are high-redshift star-forming galaxies characterized by higher star formation rates and gas fractions than their local counterparts, they also appear to host star-forming regions with significantly different physical conditions, including greater electron densities. To understand what physical mechanisms are responsible for the observed evolution of the star-forming conditions, we have assembled the largest sample of star-forming galaxies at $z \sim 1.5$ with emission-line measurements of the [O II]λλ3726, 3729 doublet. By comparing our $z \sim 1.5$ sample to local galaxy samples with equivalent distributions of stellar mass, star formation rate and specific star formation rate we investigate the proposed evolution in electron density and its dependence on global properties. We measure an average electron density of $114^{+28}_{-27}$ cm$^{-3}$ for our $z \sim 1.5$ sample, a factor of 5 greater than the typical electron density of local star-forming galaxies. However, we find no offset between the typical electron densities of local and high-redshift galaxies with equivalent star formation rates. Our work indicates that the average electron density of a sample is highly sensitive to the star formation rates, implying that the previously observed evolution is mainly the result of selection effects.

**Key words:** galaxies: evolution – galaxies: high-redshift – galaxies: ISM.

## 1 INTRODUCTION

The cosmic star formation rate (SFR) has changed significantly since the formation of the first galaxies, declining by an order of magnitude in the last 10 Gyr (Madau & Dickinson 2014). Not only did the early Universe ($z > 2$) contain a greater fraction of actively star-forming galaxies, it also hosted star-forming galaxies with considerably higher SFRs than galaxies of equivalent stellar mass ($M_*$) today (Daddi et al. 2007; Elbaz et al. 2011; Speagle et al. 2014). Although we now know that star-forming galaxies have grown in size, accumulated stellar mass and become more chemically enriched over cosmic time, we are yet to understand what mechanisms have driven the changing SFR.

To unlock the star formation history of the Universe, we need to better understand the conditions within star-forming regions. Both the ionizing sources and physical conditions of star-forming regions can be probed by measuring the strengths of rest-frame optical emission lines stemming from the ionized gas. The relative strengths of these emission lines are mainly governed by a small set of interstellar medium (ISM) properties including the chemical abundance, shape of the ionizing radiation field, ionization state and gas density (Kewley & Dopita 2002; Dopita et al. 2006a,b; Kewley et al. 2013).

Prior to the last decade, samples of rest-frame optical spectra of $z > 1$ galaxies were small, biased and only included the strongest emission lines. The lack of near-infrared (NIR) spectroscopy for high-redshift galaxies reflected the difficulty in combating the combined effects of poor CCD sensitivity, detector fringing and sky deterioration, resulting in a cosmological blind spot at $1 < z < 3$ dubbed the 'redshift desert' (Adelberger et al. 2004; Steidel et al. 2004). Far from being an arid landscape, the redshift desert is an important epoch in the history of star formation and galaxy assembly in the Universe. Not only did the SFR density peak around $z \sim 2$ (Hopkins & Beacom 2006; Madau & Dickinson 2014) but the majority of the stellar mass and heavy elements in today's Universe were produced in the redshift desert (Dickinson et al. 2003; Fontana et al. 2003; Rudnick et al. 2003; Kobulnicky & Kewley 2004; Drory et al. 2005; Zahid et al. 2014).

Thanks to the advent of NIR multi-object spectroscopy on 8–10 m telescopes, large samples of $z > 1$ star-forming galaxies with rest-frame optical emission-line measurements are now being assembled. The ensuing studies suggest that high-redshift star-forming galaxies exhibit emission-line properties that are atypical of the local star-forming galaxy population. In particular, there is increasing evidence for a significant enhancement of emission-line ratios including [O III]λλ4959, 5007/[O II]λλ3726, 3729 and [O III]5007/H $\beta$ at high redshift (e.g. Hainline et al. 2009b; Kewley et al. 2013; Steidel

★ E-mail: melanie.kaasinen@anu.edu.au (MK): fuyan.bian@anu.edu.au (FB)
† Stromlo Fellow.

© 2016 The Authors
Published by Oxford University Press on behalf of the Royal Astronomical Society

Downloaded from https://academic.oup.com/mnras/article/465/3/3220/2417054 by Library user on 15 March 2021

et al. 2014; Hayashi et al. 2015; Shapley et al. 2015). The observed changes in emission-line ratios indicate that at least some of the conditions within star-forming regions must have evolved since the early Universe.

It is still unclear which physical properties of star-forming regions are driving the observed changes in emission-line ratios. Although high-redshift galaxies are less chemically enriched than local galaxies of the same stellar mass (Kobulnicky & Kewley 2004; Cullen et al. 2014; Zahid et al. 2014), the elevated line ratios cannot be solely attributed to lower chemical abundances (e.g. Hainline et al. 2009a; Kewley et al. 2013; Masters et al. 2014; Nakajima & Ouchi 2014; Steidel et al. 2014). Other possible contributors include higher ionization parameters and/or electron densities (e.g. Brinchmann, Pettini & Charlot 2008; Masters et al. 2014; Shirazi, Brinchmann & Rahmati 2014b; Kewley et al. 2015), harder ionizing radiation fields (Kewley et al. 2013; Steidel et al. 2014), contributions from shocks/Active Galactic Nuclei (AGN) (Groves, Heckman & Kauffmann 2006; Newman et al. 2014), a variation in the N/O ratio (e.g. Masters et al. 2014; Shapley et al. 2015) and/or selection effects (Kewley et al. 2013; Juneau et al. 2014; Masters et al. 2014; Newman et al. 2014; Cowie, Barger & Songaila 2016; Dickey et al. 2016).

To resolve the current deadlock, we have assembled a sample of star-forming galaxies at high redshift ($z \sim 1.5$) with the 'full suite' of rest-frame optical-line flux measurements (i.e. [O II], H$\beta$, [O III], H$\alpha$ and [N II]). Thanks to the Fibre Multi-Object Spectrograph-COSmic evOlution Survey (FMOS-COSMOS) survey (Silverman et al. 2015; Kashino et al. 2016), measurements of H$\beta$, [O III], H$\alpha$ and [N II] are already available for a large ($\sim$500) sample of galaxies at $z \sim 1.5$. We complement the existing FMOS data with high-resolution ($R \sim 2000$) spectroscopy of the [O II]$\lambda\lambda$3726, 3729 doublet. Previous studies at $z \sim 1.5$ were either statistically insignificant, plagued by selection effects or lacked the necessary number of emission lines required to probe the conditions within star-forming regions (e.g. Liu et al. 2008; Kashino et al. 2013; Hayashi et al. 2015; Kashino et al. 2016). By gathering the largest sample of star-forming galaxies at $z \sim 1.5$ with [O II] doublet measurements, our work provides the missing link between the local Universe and recent high-redshift ($z \sim 2.3$) studies from the KBSS and MOSDEF surveys (e.g. Shapley et al. 2015; Sanders et al. 2016). Here, we present our data and measurements of the electron density.

Increasingly, high-redshift observational studies are finding evidence for elevated electron densities and/or ionization parameters (e.g. Hainline et al. 2009b; Bian et al. 2010; Masters et al. 2014; Shirazi et al. 2014a,b; Sanders et al. 2016). However, the current body of work remains inconclusive, with most studies limited by small sample sizes and/or selection effects. Because most high-redshift studies fail to take out correlations with global galaxy properties when comparing the typical electron densities and ionization parameters of high-redshift and local galaxies it remains unclear whether the enhanced electron densities and ionization parameters at high redshift are simply the byproduct of probing 'typical' star-forming galaxies with higher specific SFRs (sSFRs; SFR/M$_*$) than 'typical' local galaxies.

Recently, several studies have suggested a correlation between the electron density and/or ionization parameter of star-forming galaxies and their sSFRs (Kewley et al. 2015; Bian et al. 2016; Holden et al. 2016). We investigate the proposed correlations with global galaxy properties by comparing the electron densities of our $z \sim 1.5$ sample to three samples of local star-forming galaxies with equivalent distributions of either stellar mass, SFR or both stellar mass and SFR. By matching the local and high-$z$ ($z \sim 1.5$) samples based on their global properties, we are able to isolate the primary driver of the observed increase in the electron density.

This paper is structured as follows. In Section 2, we describe the survey design, observations and data reduction for our $z \sim 1.5$ sample. We describe the selection of the high-$z$ and local samples used in this work in Section 3 and show the global properties of these samples. In Section 4, we estimate the typical electron densities of our samples and investigate the proposed evolution with redshift. We conclude by summarizing our results in Section 5. Throughout this paper, we refer to the values of SFR, sSFR and M$_*$ consistent with a Kroupa IMF. When deriving the SFR, we adopt a $\Lambda$-CDM cosmology with $H_0 = 70\,\mathrm{km\,s^{-1}\,Mpc^{-1}}$, $\Omega_\mathrm{m} = 0.3$ and $\Omega_\Lambda = 0.7$.

## 2 OBSERVATIONS AND DATA REDUCTION

### 2.1 The COSMOS-[O II] survey

Our work is based upon a sample of star-forming galaxies from COSMOS. We derive our sample from COSMOS to take advantage of the extensive multiwavelength ground and space-based observations already at hand (Scoville et al. 2007). The 2 deg$^2$ equatorial field encompassed by the COSMOS survey is visible from most ground-based optical and IR telescopes including the Keck and Subaru telescopes (Scoville et al. 2007). A major spectroscopic survey has already been undertaken using FMOS on Subaru (PIs Sanders and Silverman, Silverman et al. 2014), resulting in H$\alpha$ detections at S/N > 3 for $\sim$900 galaxies at $1.4 < z < 1.7$. We complete the emission-line measurements for these galaxies with corresponding observations of the [O II]$\lambda\lambda$3726,3729 doublet using the DEep Imaging Multi-Object Spectrograph (DEIMOS; Faber et al. 2003) on Keck II.

Our COSMOS-[O II] survey (PI L. J. Kewley) is primarily targeted at galaxies with existing FMOS spectroscopy. All targets were identified from the COSMOS photometric catalogues (McCracken et al. 2012; Ilbert et al. 2013). Initial stellar masses for target selection were estimated based on the broad-band photometry and fitting results of LEPHARE (Arnouts & Ilbert 2011). We targeted galaxies with $\mathrm{M}_* \geq 10^{9.8}\,\mathrm{M}_\odot$ (Chabrier IMF), $\mathrm{SFR_{phot}} > 10\,\mathrm{M}_\odot\,\mathrm{yr}^{-1}$ and z(AB) magnitudes $\lesssim 24$ (SuprimeCam, $z^{++}$, $\lambda_\mathrm{c} = 9106$, Laigle et al. 2016). For further analysis, we use the latest stellar mass estimates from Laigle et al. (2016), normalized to a Kroupa IMF.

### 2.2 COSMOS-[O II] observations

Spectroscopic observations for the COSMOS-[O II] survey were conducted over two nights, UTC 2014 February 24 and 25, with DEIMOS on the Keck II telescope. We observed seven COSMOS masks, each with $\sim$150 slits. Each mask was observed three times for 20 min to optimize cosmic ray rejection. The average seeing over the two nights was $\sim$0.75 arcsec. All observations were conducted with the 600ZD grating centred at 7500Å, the OG550 filter and 1 arcsec slit width. For the $1.4 \lesssim z \lesssim 1.7$ galaxy sample in this paper, the [O II] doublet falls on the central portion of the red side (7500–9800 Å) of the DEIMOS spectrograph. The resulting spectra have a dispersion of $\sim$0.65 Å px$^{-1}$ and spectral resolution of $R \sim 2000$.

### 2.3 Data reduction

Our raw science frames were initially processed using the publicly available IDL based pipeline, SPEC2D, developed by the DEEP2 survey team (Cooper et al. 2012; Newman et al. 2013). The SPEC2D pipeline performs bias removal, flat-fielding, cosmic ray rejection,



Downloaded from https://academic.oup.com/mnras/article/465/3/3220/2417054 by Library user on 15 March 2021

slit-tilt corrections and wavelength calibration on a slit-by-slit basis (Newman et al. 2013). Sky subtraction was performed without the use of a dithering pattern. We used standard Kr, Xe, Ar and Ne arc lamps for wavelength calibration. Using SPEC2D we generated one sky-subtracted, cosmic ray cleaned two-dimensional (2D) spectrum for each slit.

Our initial [O II] sample was detected by visually inspecting the 2D spectra for [O II] emission features. For galaxies where emission lines were present, we recorded the central position on the slit of the emission feature (and, where present, the continuum) as well as an initial redshift estimate based on the observed wavelength of the [O II] doublet. Where relevant, we noted the presence of multiple emission features (from separate star-forming regions) and any data reduction problems such as sky continuum errors caused by scattered OH light from a neighbouring slit (see Newman et al. 2013). Based on the initial redshift estimates and additional notes, we selected 115 galaxies for further analysis.

We simultaneously corrected our 2D spectra for detector sensitivity and atmospheric extinction using observations of the flux standard star, DA white dwarf G191-B2B (Oke 1990). From the 1D stellar spectrum we derived a sensitivity curve, representing the convolution of the instrument response function and the atmospheric absorption. All 2D spectra were divided by the sensitivity curve to remove the effects of telluric absorption and instrument response. We derived a flux-scaling relation by applying the sensitivity curve to the 1D spectrum of the G191-B2B and matching the corrected spectrum with the absolute flux spectrum from the ESO archives. The resulting scaling relation was applied to all 2D slit spectra to generate the 2D flux calibrated spectra.

The 2D flux calibrated spectra were reduced to 1D by calculating the total flux over the effective aperture for the 'red' side of each spectrum. We define the effective aperture as the region along the length of a slit at which emission-line features or continua are detected (horizontal-dashed white lines in the upper panels of Fig. A1) and determine the size of the effective apertures by fitting the Gaussian profiles to the spatial flux distributions. We summed the flux within the effective aperture over the 'red side' of each spectrum to produce our 1D spectra (bottom panels in Fig. A1). Small changes to the size of the effective aperture had no measurable impact upon the derived 1D galaxy spectra and were therefore not considered in our error calculations.

### 2.4 Emission-line fitting

We measure the emission-line fluxes of the [O II] doublet by fitting a double Gaussian profile to a ∼35 Å window of each 1D spectrum, centred at the observed wavelength of the [O II] doublet (bottom panels in Fig. A1). Our fitting routine utilizes IDL's 'MPCURVEFIT', a Levenberg–Marquardt least-squares minimization algorithm which fits a user supplied model and returns best-fitting parameters, errors, and a measure of the overall quality of the fit. We fix the vacuum wavelengths of the doublet lines to $\lambda_1 = 3727.09$ Å and $\lambda_2 = 3729.88$ Å. To minimize the impact of OH lines our fitting routine takes into account a $1/N^2$ weighting scheme for each pixel, based on the standard deviation of the flux outside the effective aperture ($N$, blue lines in Fig. A1). Throughout, we use the $1\sigma$ error on the fit parameters combined with the covariance values returned by 'MPCURVEFIT' to estimate the errors on our parameters. The reduced chi-squared values ($\chi^2/\nu$) returned by our fitting routine are used as an indication of the goodness of the line fits and our errors are scaled accordingly for fits where $\chi^2\nu > 1$.

## 3 SAMPLE SELECTION

### 3.1 The $z \sim 1.5$ sample

Our COSMOS-[O II] survey targeted ∼430 galaxies at $1.4 \lesssim z \lesssim 1.7$, 103 of which were identified to have [O II] detections ($>2\sigma$). Of the 103 galaxies with detected [O II], 46 galaxies have corresponding H$\alpha$ detections from the FMOS-COSMOS survey. We refer to the total sample of 103 COSMOS galaxies for which we detect [O II] as the '[O II] sample' and refer to the subsample for which we have detections of both H$\alpha$ and [O II] as our '[O II]-H$\alpha$ sample'. We present the data, derived quantities, global properties and spectra of our [O II]-H$\alpha$ sample in Table A1 and Fig. A1.

We take the median stellar masses from Laigle et al. (2016), derived by fitting model spectra to the spectral energy distributions via LEPHARE (Arnouts & Ilbert 2011) following the methods outlined by Ilbert et al. (2015). To convert to a Kroupa IMF, we apply a constant scaling factor of 1.06, taken from Zahid et al. (2012). The SFRs and sSFRs of our [O II]-H$\alpha$ sample were estimated from the dust-corrected H$\alpha$ luminosities using the conversions in Murphy et al. (2011) and Hao et al. (2011) (consistent with a Kroupa IMF). Dust corrections were estimated using H$\alpha$/H$\beta$ assuming an intrinsic ratio of 2.86, consistent with Case B recombination at $T = 10^4$ K and $n_e = 100\,\mathrm{cm}^{-3}$ (Dopita & Sutherland 2003; Osterbrock & Ferland 2006), and the Cardelli, Clayton & Mathis (1989) extinction curve.

The [O II]-H$\alpha$ sample appears to be representative of the range of SFRs spanned by $z \sim 1.5$ star-forming galaxies at the same stellar masses (see Fig. 1). As in previous high-$z$ studies, our [O II]-H$\alpha$ sample exhibits higher SFRs than is typically found for local star-forming galaxies of the same stellar mass (red data versus blue contours, right-hand panel of Fig. 1). The SFRs of our [O II]-H$\alpha$ sample are mostly consistent with the main-sequence at $z \sim 1.5$ given by the best fit derived by Speagle et al. (2014); see equation (28) therein. We describe the source of the scatter within the [O II]-H$\alpha$ sample in Kaasinen et al. (in preparation).

The stellar masses and SFRs of the [O II]-H$\alpha$ sample are also consistent with those of the parent FMOS and COSMOS-[O II] samples (left-hand panel, Fig. 1). Because many of the galaxies in the COSMOS-[O II] sample do not have H$\alpha$ detections, we compare the SFRs determined photometrically by Laigle et al. (2016). The SFRs in the left- and right-hand panels of Fig. 1 are therefore not comparable (in fact there exists significant scatter in the correlation between the two). The [O II]-H$\alpha$ sample spans the stellar mass range $10^{9.6} - 10^{11.9}\,\mathrm{M}_\odot$ and SFR range $3 - 150\,\mathrm{M}_\odot\,\mathrm{yr}^{-1}$ with a median stellar mass of $10^{10.7}\,\mathrm{M}_\odot$ and median SFR of $15\,\mathrm{M}_\odot\,\mathrm{yr}^{-1}$. The range of sSFRs spanned by the [O II]-H$\alpha$ sample is $0.04 - 7.3\,\mathrm{Gyr}^{-1}$, with a median sSFR of $0.4\,\mathrm{Gyr}^{-1}$.

### 3.2 Local comparison samples

To investigate the evolution in electron density we compare our $z \sim 1.5$ [O II]-H$\alpha$ detected sample to three local comparison samples, matched according to their global properties. Previous high-redshift observational studies (e.g. Rigby et al. 2011; Sanders et al. 2016) fail to take into account the evolution of global galaxy properties, such as the SFR, when drawing comparisons between the ISM conditions of local and high-redshift galaxies. Yet, the local star-forming galaxy population typically has far lower SFR and sSFR than the high-$z$ population to which they are compared. Because most previous studies compare significantly different populations of galaxies, it remains unclear to what extent the global attributes of galaxy



Downloaded from https://academic.oup.com/mnras/article/465/3/3220/2417054 by Library user on 15 March 2021

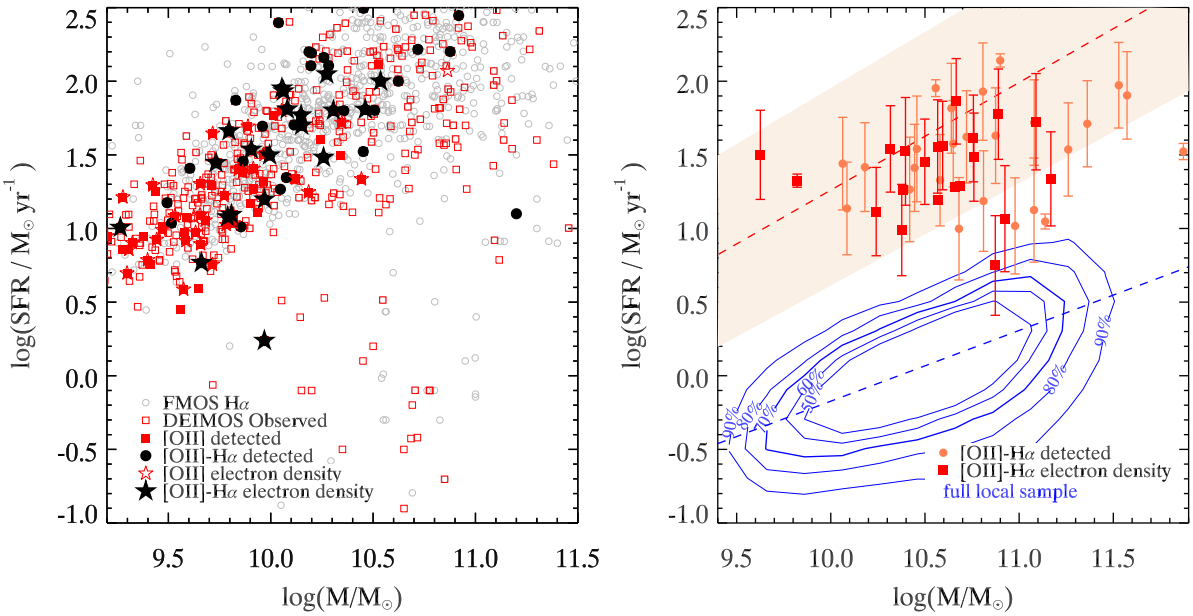


**Figure 1.** SFR versus $M_*$ for the high-$z$ samples discussed in this work. Left-hand panel: median log (SFR) and log($M_*$) determined by Laigle et al. (2016) based on fits to photometry using LEPHARE. Galaxies observed as part of the FMOS-COSMOS (open grey circles) and COSMOS-[O II] surveys (open red squares) are compared to [O II]-detected (filled-red squares) and [O II]-H$\alpha$ detected (filled-black circles) subsamples. The samples for which electron densities could be determined are shown as stars. Right-hand panel: H$\alpha$ based star formation rates for the $z \sim 1.5$ [O II]-H$\alpha$ sample (filled-orange circles), the electron-density subsample (red squares) and local SDSS star-forming galaxies (blue contours, showing the distribution density). The local and $z \sim 1.5$ samples are compared to the main-sequence fits at $z \sim 1.5$ (red dashed and filled pink) and $z \sim 0$ (blue dashed) given by equation (28) of Speagle et al. (2014). Note that the left- and right-hand panels are not directly comparable due to differences between photometric and H$\alpha$ based SFRs.

samples are responsible for driving the observed evolution of ISM conditions. We address this issue by selecting three local comparison samples matched to our primary high-$z$ sample according to the global properties commonly used to design galaxy surveys (i.e. $M_*$ and SFR).

We derive our local comparison samples from the Sloan Digital Sky Survey (SDSS; York et al. 2000) Data Release 7 (Abazajian et al. 2009) catalogue. The emission-line measurements, stellar masses and SFRs are taken from the MPA-JHU catalogues (Kauffmann et al. 2003; Brinchmann et al. 2004; Tremonti et al. 2004). SDSS SFRs are estimated from the H$\alpha$ luminosities after correcting for aperture loss of the SDSS fibres and dust extinction based on H$\alpha$/H$\beta$. Although the SFRs are based on a Kroupa IMF, SDSS stellar masses are based on a Chabrier IMF. We therefore normalize to a Kroupa IMF (as described for our high-$z$ sample). To estimate the effects of dust extinction and derive ISM conditions we require [O II]$\lambda$3727, H$\beta$, [O III]$\lambda$5007, H$\alpha$, [N II]$\lambda$6583 and [S II]$\lambda\lambda$6716, 6731 to be detected at a S/N >3. We reject AGN, based on the standard optical-line ratios, using the Kewley et al. (2001) maximum starburst criteria and reduce systematic errors from aperture effects by selecting galaxies at $z > 0.04$ (Kewley, Jansen & Geller 2005). To ensure that we select galaxies that are representative of the local Universe we limit the redshift to $z \leq 0.1$. These imposed constraints result in a sample of 123 652 local star-forming galaxies which we refer to as the 'full local sample'.

We select three 'matched' samples from the full local sample by matching an ensemble of local counterparts to each galaxy in our $z \sim 1.5$ [O II]-H$\alpha$ sample. Our first local comparison sample is matched solely on stellar mass, without applying any constraints to the SFR. We refer to this sample as the $M_*$-matched sample (top row, Fig. 2). To create the $M_*$-matched sample, we require the stellar mass of the local counterparts to be within 0.2 dex of each high-$z$ galaxy. Conversely, for our second local comparison sample we require the SFRs of the high-$z$ galaxies and local counterparts to be consistent within 0.2 dex but impose no constraints on $M_*$. We refer to the second sample as the SFR-matched sample (middle row, Fig. 2). We derive our third local sample, the $M_*$-and-SFR-matched sample, by combining constraints on the stellar mass and SFR. To select the $M_*$-and-SFR-matched sample we require that the sSFR of the high-$z$ sample and local counterparts are consistent to within 0.2 dex and both the $M_*$ and SFR are consistent to within 0.3 dex.

To ensure that the statistical properties of the matched, local and high-$z$ samples are equivalent, we select the same number of local counterparts for each high-$z$ galaxy. Although there were more than 50 local galaxies with equivalent $M_*$ for each high-$z$ galaxy, a greater sample size did not result in a change in the electron-density distribution. We therefore limit the size of our $M_*$-matched sample, by randomly selecting 50 local galaxies for each high-$z$ galaxy. In contrast, the number of local counterparts in both the SFR-matched and the $M_*$-and-SFR-matched samples is limited by the rarity of high SFR galaxies in the local SDSS sample. We only find seven local counterparts for our highest SFR high-$z$ galaxy and thus select seven local galaxies at random for the remainder of our sample. Because we impose further constraints to select the $M_*$-and-SFR-matched sample we are limited to five local counterparts for each high-$z$ galaxy.

The three matched local samples have significantly different distributions of $M_*$, SFR and sSFR (see Fig. 2). Both the $M_*$-matched-and-SFR-matched local samples have significantly lower sSFRs than our high-$z$ sample, reflecting the evolution of the main star-forming sequence ($M_*$ versus SFR) with redshift (e.g. Speagle et al. 2014). As shown in Fig. 2, most of the local galaxies with equivalent $M_*$ to galaxies in the high-$z$ sample have lower SFRs. Conversely, most of the local galaxies with equivalent SFRs to our

Downloaded from https://academic.oup.com/mnras/article/465/3/3220/2417054 by Library user on 15 March 2021

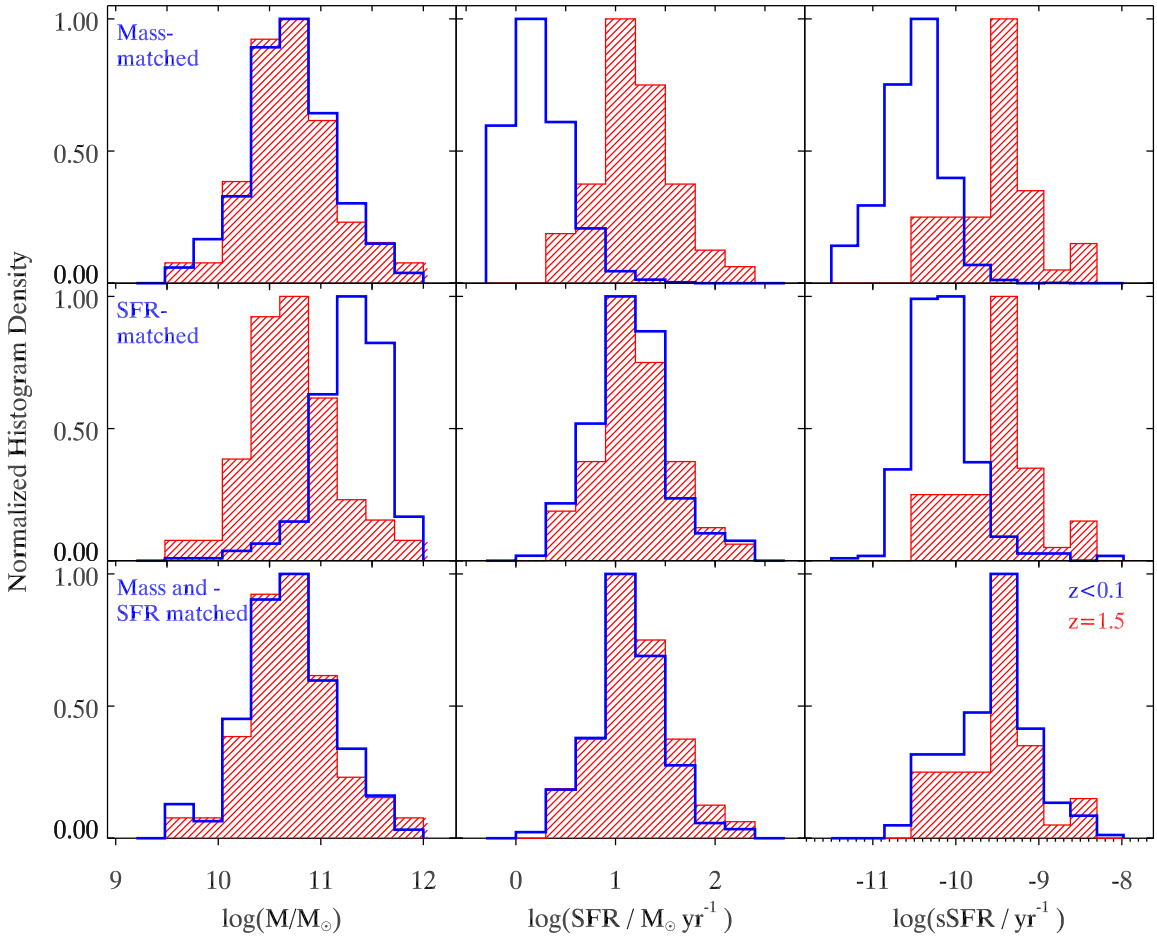


**Figure 2.** Comparison between the distributions of $M_*$ (left), SFR (centre) and sSFR (right) for the matched local comparison samples (blue outline) and $z \sim 1.5$ [O II]-H$\alpha$ sample (red line fill). Top row: $M_*$-matched local sample. Middle row: SFR-matched local sample. Bottom row: $M_*$-and-SFR-matched local sample.

high-z sample (of which there are far fewer) are more massive than our high-z galaxies. We note that because of the rarity of high SFR local galaxies and the selection criteria imposed, there is a significant overlap between the SFR- and the $M_*$-and-SFR-matched samples.

## 4 ELECTRON DENSITIES

The electron density is a useful diagnostic of the pressure and density of the gas within star-forming regions. Greater electron densities may help to drive the elevated emission-line ratios observed at high redshift by increasing the rate of collisional excitation (e.g. Kewley et al. 2013; Shirazi et al. 2014b; Sanders et al. 2016). The electron density can be estimated using the ratio of an emission-line doublet arising from a single species in which the two energy levels have nearly the same excitation energy but different collisional strengths and radiative probabilities (Veilleux & Osterbrock 1987). Two electron-density sensitive doublets, [O II]$\lambda\lambda$3726, 3729 and [S II]$\lambda\lambda$6716, 6731, may be accessed via rest-frame optical spectra.

### 4.1 Methods

We rely on different emission-line doublets to estimate the electron densities of our local and high-$z$ samples because of the difference in resolution elements. The $z \sim 1.5$ DEIMOS spectra have a spectral resolution of $R \sim 2000$, which is sufficient to fully resolve the [O II]$\lambda\lambda$3726,3729 doublet (separated by ~6.8 Å at $z \sim 1.5$). In contrast, local SDSS spectra have a spectral resolution of $R = 1800$ at the [O II] wavelength (York et al. 2000), corresponding to a resolution element of ~2.1 Å. Because the SDSS spectral resolution cannot fully resolve the 2.78 Å separation of the components of the [O II] doublet, we rely on the [S II]$\lambda\lambda$6716,6731 doublet to estimate the electron density of the local sample. As shown by Sanders et al. (2016), the electron densities determined from [S II] and [O II] for individual H II regions are highly consistent. Because the lines in both doublets are sufficiently close in wavelength, no correction for dust extinction is necessary.

We calculate the electron densities of our local and high-$z$ samples using the functional form derived in Sanders et al. (2016),

$$n_e(R) = \frac{cR - ab}{a - R}\,, \tag{1}$$

where $R$ is ratio between the peak fluxes of the two emission-line doublet components, $n_e$ is the electron density in cm$^{-3}$ and $a$, $b$ and $c$ are the coefficients which best fit the numerical solutions to the relative populations of the doublets. We provide the coefficients and limiting line ratios derived by Sanders et al. (2016) in Table 1.

The relationships derived by Sanders et al. (2016) are the result of a detailed balance of transitions for each of the five energy levels



Downloaded from https://academic.oup.com/mnras/article/465/3/3220/2417054 by Library user on 15 March 2021

**Table 1.** Coefficients and limiting line ratios for [O II] and [S II] applied to equation (1).

| Ratio | $a$ | $b$ | $c$ | $R^1_{\rm min}$ | $R^2_{\rm max}$ |
|---|---|---|---|---|---|
| [O II]λ3726/λ3729 | 0.3771 | 2468 | 638.4 | 0.3839 | 1.4558 |
| [S II]λ6716/λ6731 | 0.4315 | 2107 | 627.1 | 0.4375 | 1.4484 |

[1]Theoretical minimum line ratio calculated in the high-density limit of $10^5$ cm$^{-3}$.
[2]Theoretical maximum line ratio calculated in the low-density limit of 1 cm$^{-3}$.

approximated for the $O^+$ and $S^+$ ions. Calculating the emission-line ratio corresponding to a given density requires accurate transition probabilities and collision strengths. Sanders et al. (2016) rely on the most up-to-date atomic data taking transition probabilities for both [O II] and [S II] from the NIST MCHF data base (Fischer 2014) and collision strengths from Tayal (2007) and Tayal & Zatsarinny (2010) for [O II] and [S II], respectively. The methods and atomic data implemented by Sanders et al. (2016) are validated by the one-to-one relation between the electron densities of local H II regions derived from [O II] and [S II].

The functional form derived by Sanders et al. (2016) incorporates a number of assumptions. By using their relation, we assume that all of the star-forming galaxies in our samples can be modelled as H II regions consisting of a fully ionized gas with an isobaric density distribution. We thereby assume that the electron density is directly proportional to the H II region pressure and that these regions have an electron temperature of $10^4$ K (see Dopita et al. 2006b for a discussion). Given the dependence of the collision strength upon temperature, this assumption may lead to an overestimation in the electron density for metal-rich galaxies (and vice versa for metal-poor galaxies). We note that the uncertainty introduced by this assumption is significantly less than the typical measurement error for individual galaxies.

### 4.2 Electron-density samples

Small changes in the line fluxes can have a significant impact upon the inferred electron density, especially at low densities where the line ratio is close to unity. It is therefore crucial that the doublets used to infer electron densities are free of any contamination from sky lines. We visually inspect all of our [O II] doublets and remove any spectra showing evidence of skyline contamination in the wavelength range of the doublet (starred galaxies in Table A1). In addition, we require S/N > 5 for the line fluxes of both [O II] components and use the covariance of the line fluxes of the doublets to ensure that we only select galaxies with S/N > 3 for the flux ratio.

Our applied selection cuts result in 57 [O II] and 21 [O II]-H$\alpha$ high-z galaxies for which we calculate electron densities. For the one galaxy resolved into two separate star-forming regions (Deimos ID: 'D416912'), we separately calculate the electron density of each region and average the result. We find no evidence for AGN contamination in either the [O II] or [O II]-H$\alpha$ $z \sim 1.5$ samples for which we calculate the electron densities, based on the [O III]/H$\beta$ and [N II]/H$\alpha$ diagnostic line ratios (Kewley et al. 2001) and lack of X-ray detections. Our [O II]-H$\alpha$ electron-density subsample has a median stellar mass of $10^{10.59}$ M$_\odot$, a median SFR = 28 M$_\odot$ yr$^{-1}$ and median sSFR = 0.7 Gyr$^{-1}$ (note that these values differ slightly from the medians for the larger [O II]-H$\alpha$ sample). To ensure a fair comparison, we only present the electron densities for local galaxies matched to the subsample of high-$z$ [O II]-H$\alpha$ detected galaxies for which we estimate electron densities.

**Table 2.** Median line ratios and typical electron densities of the local and high-$z$ samples.

| High-$z$ samples | | |
|---|---|---|
| Sample name | Median [O II]λ3726/λ3729 | $n_{\rm e}$ (cm$^{-3}$) |
| [O II] detected | $1.32 \pm 0.02$ | $90^{+17}_{-15}$ |
| [O II] − H$\alpha$ detected | $1.29 \pm 0.03$ | $114^{+28}_{-27}$ |
| **Local samples** | | |
| Sample name | Median [S II]λ6716/λ6731 | $n_{\rm e}$ (cm$^{-3}$) |
| Full local sample | $1.4081 \pm 0.0002$ | $26.8^{+0.2}_{-0.2}$ |
| $M_*$-matched | $1.406 \pm 0.003$ | $28^{+2}_{-2}$ |
| SFR-matched | $1.310 \pm 0.004$ | $98^{+4}_{-4}$ |
| $M_*$-and-SFR-matched | $1.312 \pm 0.006$ | $98^{+5}_{-5}$ |

### 4.3 Electron densities at $z \sim 0$ and $z \sim 1.5$

We present both the distributions and 'typical' values of the electron density for each of our samples in Fig. 3. Galaxies with line ratios above the theoretical maximum are assigned limits in the low-density (<10 cm$^{-3}$) regime. To avoid confusion, in Figs 3 and 4, we assign galaxies with line ratios above the theoretical maximum an electron density of 1 cm$^{-3}$ (noting that ratios close to the maximum theoretical line ratio can result in densities <10 cm$^{-3}$). Although a significant proportion of galaxies fall below the low-density limit, we find no galaxies with electron densities in the high-density regime.

Because most of the samples contain a significant fraction of galaxies below the low-density limit, we avoid averaging electron densities. Instead, we determine the 'typical' electron density of each sample using the median line ratio and applying equation (1). We estimate the uncertainty on the median line ratio via a resampling technique. For each iteration, we perturb the emission-line ratios according to their uncertainties and take the median of the new sample. We perform this process 1000 times to build a well-sampled distribution of median values. The reported lower and upper uncertainties of the line ratios correspond to the 15.8th and 84.2th percentile values, respectively, of the cumulative distribution function of the median. Lower and upper uncertainties on the typical electron density are determined by converting the uncertainties on the median line ratio to electron densities where the upper (lower) uncertainty in the line ratio corresponds to the lower (upper) uncertainty in the density. The median line ratios and typical electron densities of the local and high-$z$ samples are provided in Table 2.

The combined effects of redshift and spectral resolution force us to use different doublets to determine the electron densities of the local and high-$z$ samples. Because [S II] has a significantly lower ionization energy than [O II] (10.36 eV and 13.61 eV, respectively), it can exist at greater nebular distances (fig. 2, Levesque et al. 2010 and fig 4. Mesa-Delgado et al. 2011), sometimes extending well into the diffuse ISM. We expect the diffuse ISM to have a negligible effect on the integrated line ratios because we are measuring luminosity-weighted average emission-line spectra, which are dominated by the brightest HII regions. Integrated measurements of H II regions have demonstrated that the [S II] and [O II] derived densities are consistent (e.g. Sanders et al. 2016), thereby supporting our work.

Downloaded from https://academic.oup.com/mnras/article/465/3/3220/2417054 by Library user on 15 March 2021

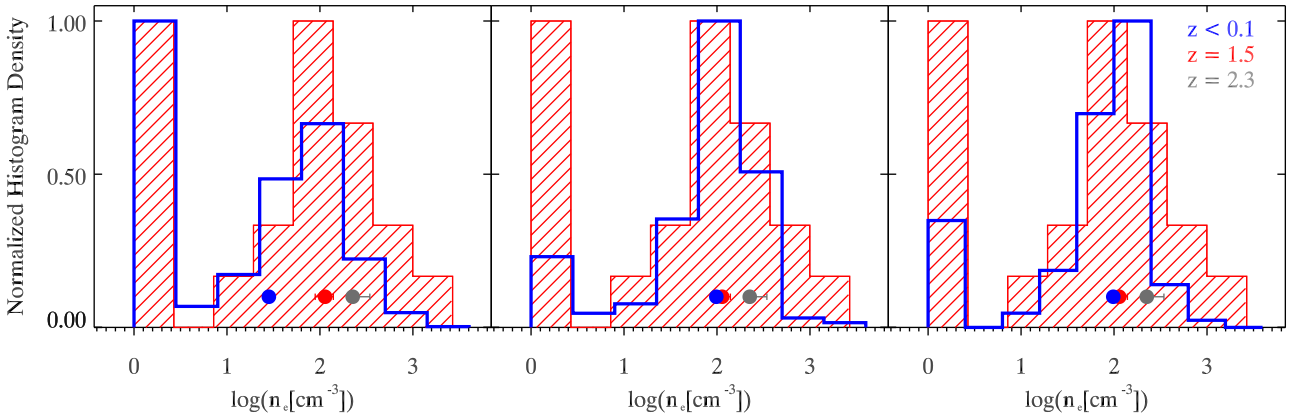


**Figure 3.** Distribution of the electron densities for our $z \sim 1.5$ [O II]-H$\alpha$ sample (red line fill), and local comparison samples matched to high-$z$ galaxies for which we determine the electron densities (blue outline). The $M_*$-, SFR- and $M_*$-and-SFR-matched local comparison samples are shown in the left-hand, middle and right-hand panels, respectively. For each panel, the typical electron density of the matched local comparison sample (filled blue circle) is compared to the typical electron density of our $z \sim 1.5$ [OII]-H$\alpha$ sample (filled-red circle) and the electron density of the $z \sim 2.3$ sample from Sanders et al. (2016) (filled-grey circle).

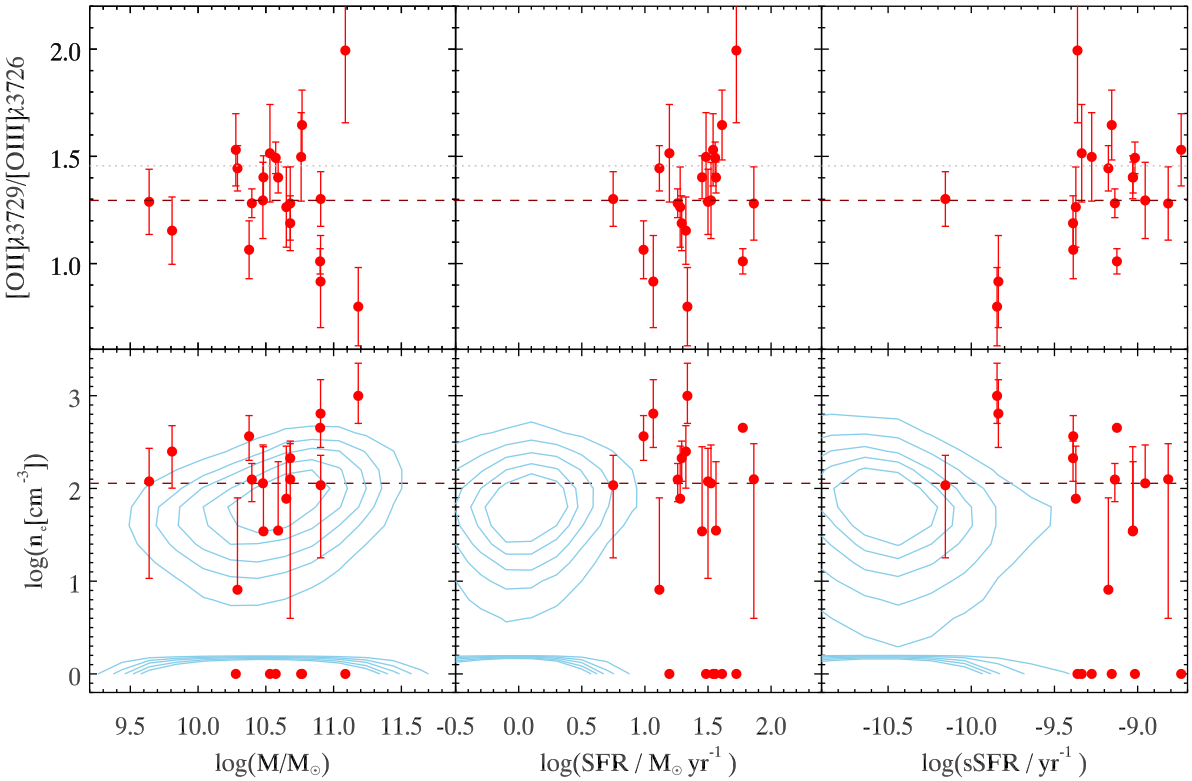


**Figure 4.** [O II]$\lambda$3726/$\lambda$3729 (top) and log ($n_e$) (bottom) as a function of $M_*$ (left), SFR (middle) and sSFR (right) for the $z \sim 1.5$ [O II]-H$\alpha$ detected sample. The light-blue contours in the bottom row show the regions encompassed by 50 per cent, 60 per cent, 70 per cent, 80 per cent and 90 per cent of the full local SDSS sample. The median [O II]$\lambda$3726/$\lambda$3729 and typical electron density are indicated by the red-dashed lines in the upper and lower row, respectively. The maximum theoretical [O II]$\lambda\lambda$3726/3729 is indicated in the top row by the dotted-grey lines.

Although individual [S II] densities could not be derived for our high-$z$ sample, Kashino et al. (2016) have determined the [S II] ratio of the stacked spectra of 701 FMOS galaxies with H$\alpha$ detections at S/N > 3, of which our [O II]-H$\alpha$ sample is a subsample. Their stacked spectra yield an average [S II] ratio of 1.21 ± 0.1, which translates to an electron density of $193^{+121}_{-93}$ cm$^{-3}$, using the methods presented here. This electron-density estimate is higher than the typical electron density of our [O II]-H$\alpha$ sample ($114^{+28}_{-27}$ cm$^{-3}$), but consistent within the uncertainties. If this offset applies to the individual galaxies of our [O II]-H$\alpha$ sample, it would enhance the difference between the high-$z$ and $M_*$-matched local sample. However, it is still unclear how well the electron density of the stacked data set reflects the mean electron density of the FMOS galaxies, especially for our subsample.



Downloaded from https://academic.oup.com/mnras/article/465/3/3220/2417054 by Library user on 15 March 2021

### 4.4 Electron density versus redshift

Our results suggest that the elevated electron densities measured at high redshift are a consequence of probing populations of galaxies with far greater star formation activity than is typical of the local Universe. We measure a typical electron density of 27 $cm^{-3}$ for our full sample of 123 652 local star-forming galaxies, consistent with the $\sim$20 $cm^{-3}$ found by Sanders et al. (2016) and Bian et al. (2016). As found in previous high-redshift studies (Masters et al. 2014; Shirazi et al. 2014b; Steidel et al. 2014; Sanders et al. 2016), the typical electron density of our high-$z$ sample is significantly greater ($\sim$5 $\times$) than that of the local galaxy population. The same offset is recovered for local and high-$z$ samples matched in stellar mass only. However, we find no significant difference between the typical electron densities of local and high-$z$ samples with equivalent SFRs ($98^{+5}_{-5}$ $cm^{-3}$ versus $114^{+28}_{-27}$ $cm^{-3}$, respectively).

Our findings appear to contradict the work of Shirazi et al. (2014b), who recover a significant difference between the electron densities of their $M_*$-and-SFR-matched local and high-$z$ samples. The conflicting results are most likely to be the result of the different methods employed to estimate electron densities. Shirazi et al. (2014b) measure the electron densities of their local sample using the [S II] ratio and derive the electron density for each corresponding high-$z$ galaxy by applying a scaling factor based on the ratio between the ionization parameters of the matched local and high-$z$ galaxies. In contrast, we directly determine the electron density for the local and high-$z$ samples, based on measured doublet ratios. We separately investigate the ionization parameter in Kaasinen et al. (in preparation) to determine whether we find the same dependence on SFR as for the electron density.

### 4.5 Electron density versus global galaxy properties

Our work indicates that the previously observed evolution in electron density is related to the evolution of SFR rather than $M_*$. Recent high-redshift studies which measure high electron densities, probe samples of galaxies with higher SFRs than typically found at $z < 1.5$. Both Steidel et al. (2014) and Masters et al. (2014) estimate a typical electron density of $\sim$243 $cm^{-3}$ for their $z \sim 2.3$ and $z \sim 1.85$ samples which have the median SFRs of 20 $M_\odot$ $yr^{-1}$ and 25 $M_\odot$ $yr^{-1}$, respectively. Similarly, Sanders et al. (2016) measure a typical electron density of $\sim$225 $cm^{-3}$ for their $z \sim 2.3$ [O II] detected sample which has a median SFR of $\sim$30 $M_\odot$ $yr^{-1}$. Shimakawa et al. (2015) measure a typical electron density of $\sim$290 $cm^{-3}$ for their sample of 14 H$\alpha$ emitters at $z \sim 2.5$ for which the median SFR is $\sim$100 $M_\odot$ $yr^{-1}$. Although the SFRs of these high-$z$ samples differ significantly from those of the local comparison samples, the stellar mass ranges are directly comparable. Thus, it would appear as though variations in electron density are driven mainly by differences in SFR.

We investigate how the doublet ratios and electron density vary with global galaxy properties both graphically (Fig. 4) and by performing a Spearman rank correlation test for each parameter space. To determine the extent to which the variables are related we measure the strength of the monotonic relationship for each pairing via the Spearman rank coefficient, $\rho_s$, and consider the significance of the correlation via $\alpha$, the likelihood of $\rho_s$ being found by chance if the two variables are uncorrelated. For our high-$z$ [O II]-H$\alpha$ sample there is neither graphical nor statistical evidence for any correlations (i.e. $\alpha > 0.15$ in all cases). These findings contradict the significant correlation (4$\sigma$ level) between the electron density and sSFR found by Shimakawa et al. (2015). However, given the limited range in global properties and extent of the uncertainty for each individual measurement, our high-$z$ sample is likely to be too small to recover any underlying correlations.

Unlike the high-$z$ sample, the local samples exhibit weak but significant correlations. For each of the local samples (listed in Table 2), we find a weak negative Spearman's correlation ($\rho_s \sim -0.1$) between the [S II] line ratio and $M_*$, which translates into a weak positive correlation between the electron density and stellar mass ($\rho_s \sim 0.2$). Additionally, each of the local samples exhibits a weak negative correlation between the [S II] ratio and SFR which translates to a weak positive correlation between the electron density and SFR. The $\rho_s$ values describing the relationship between the electron density and SFR are greater for the local samples matched in SFR ($\rho_s \sim 0.4$) than for the full and $M_*$-matched samples ($\rho_s \sim 0.15$). Further differences between the samples are apparent when investigating the relationship between the electron density and sSFR. Both the full and $M_*$-matched local samples exhibit no correlation between the electron density and sSFR, whereas the samples matched in SFR exhibit weak positive correlations ($0.1 < \rho_s < 0.3$). The weakness of the monotonic relationships and differences between samples are also indicated by the contours for the full local sample shown in Fig. 5. At high SFR ($\log(\mathrm{SFR}/\,M_\odot\,yr^{-1}) > 0.5$) and sSFR ($\log(\mathrm{sSFR}/\,yr^{-1}) > -10$), the range of likely electron densities is smaller and offset to higher values.

We extend our investigation into the dependence of the electron density on global properties using the full sample of 123 652 local star-forming galaxies. Rather than separately investigating the correlation between the electron density and each global property, we compare the electron densities of different bins of SFR and $M_*$. For each bin, we compute the typical electron density (as described in Section 4.1), determine the fraction of galaxies in the low-density regime and count the total number of galaxies to account for sample characteristics (Fig. 5, left-hand, middle and right-hand panels, respectively). We also show lines of constant sSFR (Fig. 5, red dot–dashed and dashed lines). We require at least 20 galaxies per SFR and $M_*$ bin but impose no upper limit on the number. Bins where $-10 < \log(\mathrm{sSFR}/\,yr^{-1}) < -10.7$ and $10.2 < \log(M_*/\,M_\odot) < 11.2$ contain the greatest number of galaxies, reflecting the characteristics of SDSS as well as our selection criteria.

The electron density of the bins of local galaxies appears to be more strongly dependent on the SFR than the stellar mass. For each $M_*$ bin, the typical electron density increases with SFR above $\sim\log(\mathrm{sSFR}/\,yr^{-1}) > -10.7$ (left-hand panel in Fig. 5). Furthermore, the fraction of galaxies with electron densities in the low-density regime decreases dramatically with increasing SFR, above $\log(\mathrm{sSFR}/\,yr^{-1}) > -10.7$. This dependence on SFR (and sSFR) is also apparent for the matched local samples. Approximately 40 per cent of both the full local sample and $M_*$-matched sample have electron densities in the low-density limit, whereas $\sim$15 per cent of the samples matched in SFR exhibit electron densities in the low-density regime. Thus, the previously observed increase in electron density at high redshift may be driven by the decreasing fraction of galaxies within the low-density regime for populations with higher SFRs.

The dependence of the electron density of a sample on the SFR may reflect a correlation between the electron density and SFR density. Because it is observationally challenging to determine the SFR volume density ($\rho_{\mathrm{SFR}}$) for galaxies other than our own, the SFR relative to the size of a galaxy is commonly measured via the SFR surface density ($\Sigma_{\mathrm{SFR}}$). Recently, studies have found strong evidence

Downloaded from https://academic.oup.com/mnras/article/465/3/3220/2417054 by Library user on 15 March 2021

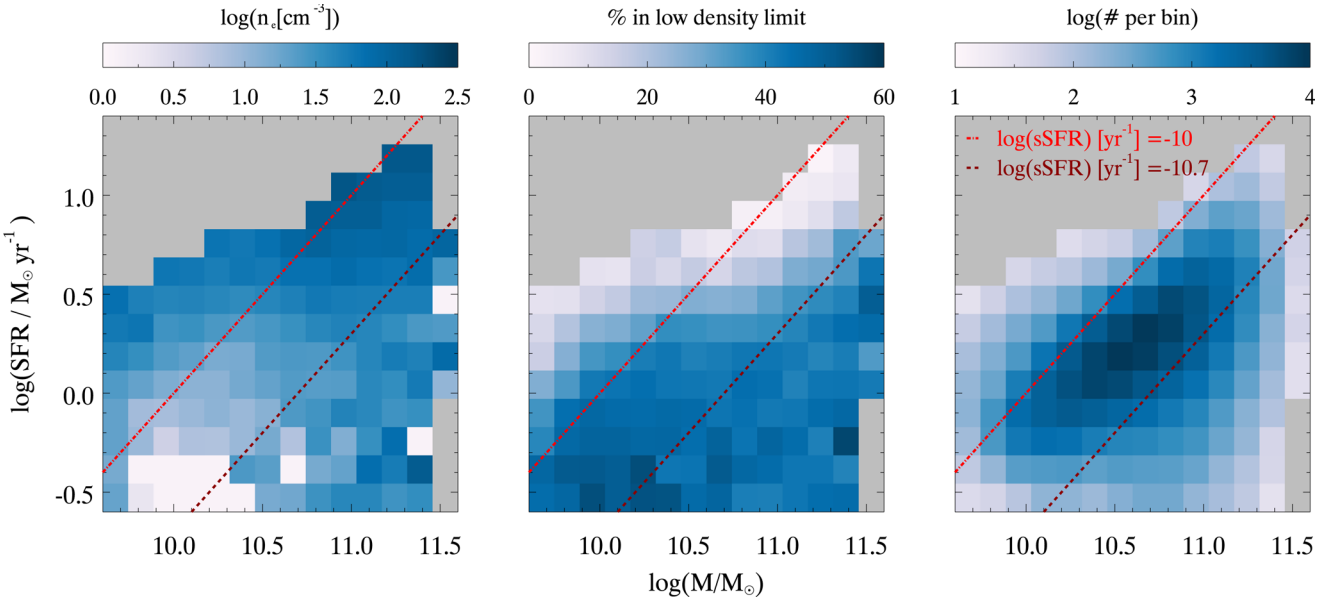


**Figure 5.** Electron density as a function of SFR and $M_*$ in local SDSS galaxies. Locii of constant sSFR are overplotted in orange and dark red for $\log(\mathrm{sSFR}/\mathrm{yr}^{-1}) > -10$ and $\log(\mathrm{sSFR}/\mathrm{yr}^{-1}) > -11$, respectively. Left-hand panel: typical electron density for each bin of ≥20 galaxies. Middle panel: fraction of galaxies in each bin with [S II]λ6716/λ6731 above the theoretical maximum i.e. fraction of galaxies in the low density regime. Right panel: Number of galaxies per bin.

for a correlation between the global $\Sigma_{\mathrm{SFR}}$ and electron density of star-forming galaxies (Shimakawa et al. 2015; Bian et al. 2016). Although we lack the spatial information required to measure the size, and therefore $\Sigma_{\mathrm{SFR}}$, for our $z \sim 1.5$ sample we note that our high-$z$ sample is unlikely to be biased towards greater galaxy sizes than the local population (e.g. van der Wel et al. 2014). We therefore expect our high-$z$ sample to have a greater average $\Sigma_{\mathrm{SFR}}$ than the local population and at least equivalent $\Sigma_{\mathrm{SFR}}$ to the local samples matched in SFR. The same argument should extend to $\rho_{\mathrm{SFR}}$ since the growth in galaxy size should be independent of the viewing angle.

There are a number of physical mechanisms by which a high SFR density may result in an enhanced average electron density. A higher SFR density means an increased number of massive, young stars per unit volume. The increased number density of massive, young, stars results in a greater energy input to H II regions, via processes such as stellar winds and shocks, increasing both their pressure and electron density (Groves et al. 2008; Krumholz & Matzner 2009). Additionally, the observed correlation between the SFR density and electron density may ensue as a result of the direct scaling between the gas surface density ($\Sigma_{\mathrm{gas}}$) and $\Sigma_{\mathrm{SFR}}$ (e.g. Kennicutt 1998; Kennicutt & Evans 2012). Increased molecular gas densities may lead to higher atomic hydrogen densities within H II regions, which are embedded in molecular gas clouds. Because the electron density scales with the number density of atomic hydrogen (e.g. Dopita & Sutherland 2003; Dopita et al. 2006a,b; Kewley et al. 2013) it may also be sensitive to the gas density. Thus, the high $\Sigma_{\mathrm{gas}}$ of high-$z$ galaxies (e.g. Tacconi et al. 2010; Genzel et al. 2013) would be expected to increase both the SFR and electron density.

In the previous arguments, we assumed that the observed emission-line fluxes stem predominantly from H II regions and that the estimated electron densities are therefore reflective of the average H II region electron density for each galaxy. But, studies on local galaxies show that 20–40 per cent of the total galactic Hα luminosity stems from the diffuse ISM, and possibly a larger fraction of the [O II] and [S II] emission (Dopita & Sutherland 2003; Haffner et al. 2009, and references therein). Most studies of the diffuse ISM (see Haffner et al. 2009) do not report any evidence for a correlation between SFR (or Hα luminosity) and the fraction of the emission stemming from the diffuse ISM, suggesting that the diffuse emission may affect our high-$z$ and local samples. Confirming the effects of contamination by diffuse emission will only be achieved via deeper observations and high physical resolution integral field unit (IFU) observations of both high- and low-$z$ galaxies.

## 5 SUMMARY

We have presented the data and first results from the COSMOS-[O II] survey. Our survey is designed to complement the FMOS-COSMOS survey (Kashino et al. 2013; Silverman et al. 2015; Zahid et al. 2014; Kashino et al. 2016) by measuring the flux of the [O II] doublet for galaxies with H- and J-long observations. As shown in this work, our data represent a critical resource for probing the ionization state of star-forming regions at $z \sim 1.5$. Without the [O II] doublet, we cannot accurately diagnose the electron density, ionization parameter or metallicity of star-forming regions.

We have investigated the average electron density of star-forming galaxies at $z \sim 1.5$ and made comparisons to local star-forming galaxies. Of the 103 galaxies at $z \sim 1.5$ with significant [O II] detections, a subsample of 46 have measured Hα. We use this subsample to explore the effects of $M_*$ and SFR on electron density. To measure the electron density, we select a subsample with high signal-to-noise ratio (S/N>3) for both components of the [O II] doublet and for which there is no evidence of skyline contamination. We measure a median [O II]λ3726/λ3729 of 1.29 ± 0.03 for our $z \sim 1.5$ [O II]-Hα detected sample, corresponding to a typical electron density of $114^{+28}_{-27}\,\mathrm{cm}^{-3}$. This typical electron density is consistent with recent high-$z$ ($1.8 < z < 2.5$) studies as well as the



Downloaded from https://academic.oup.com/mnras/article/465/3/3220/2417054 by Library user on 15 March 2021

electron density found by Kashino et al. (2016) for the parent H$\alpha$ detected FMOS-COSMOS sample.

We find strong evidence that the high electron densities measured for high-redshift galaxies are the result of the evolving global SFR. Our $z \sim 1.5$ sample exhibits a typical electron density $\sim$5 $\times$ that of the 'typical' local star-forming galaxy population and a local sample matched in stellar mass. But, we find no such evolution in electron density when comparing local and high-$z$ galaxies with the same SFR. The dependence of the electron density on SFR is also evident within the local sample, for which we plot the typical electron density and fraction of galaxies in the low-density regime as a function of $M_*$ and SFR. The dependence we have uncovered may be the result of a correlation with the SFR surface density, reported by other studies (e.g. Shimakawa et al. 2015). However, further studies of spatially resolved galaxies at $0 < z < 2$ are required to confirm this.

Our findings indicate that the enhanced emission-line ratios observed at high redshift are, at least partly, the result of probing populations of galaxies with higher SFR and sSFR than are typical of the local Universe. Higher electron densities serve to increase emission-line ratios such as [O III]/H$\beta$, (e.g. Kewley et al. 2013). Thus, the increased star formation activity at high redshift may be reflected in enhanced ratios. The proposed correlation between emission-line ratios and sSFR has only been investigated recently. Bian et al. (2016) find evidence that local galaxies with [O III]/H$\beta$ ratios equivalent to galaxies at $z \sim 2$ have significantly higher sSFRs and electron densities than the rest of the local star-forming population. Similarly, Dickey et al. (2016) show that elevated [O III]/H$\beta$ ratios are partly driven by high sSFR, regardless of the cosmic epoch.

The exact connection between global galaxy properties and the conditions within star-forming regions remains unclear. Although the electron density is one of the key physical parameters of star-forming regions, it does not convey the full picture. To fully probe the physical conditions of star-forming regions at $z \sim 1.5$, we must also investigate their metallicities and ionization parameters. Previous studies, which sample galaxies with high star formation activity, find evidence for increased ionization parameters (Steidel et al. 2014; Shimakawa et al. 2015; Sanders et al. 2016). We will investigate the observed evolution of the ionization parameter and its dependence on global galaxy properties in Kaasinen et al. (in preparation) using the high-$z$ sample presented in this work.

## ACKNOWLEDGEMENTS

We acknowledge the data, feedback and support provided by the FMOS-COMOS team, in particular Kashino Daichi, Jabran Zahid and John Silverman. BG gratefully acknowledges the support of the Australian Research Council as the recipient of a Future Fellowship (FT140101202). LK gratefully acknowledges support from an ARC Laureate Fellowship (FL150100113). We also thank the anonymous referee for the insightful comments which greatly improved this paper.

The data presented herein were obtained at the W.M. Keck Observatory, which is operated as a scientific partnership among the California Institute of Technology, the University of California and the National Aeronautics and Space Administration. The Observatory was made possible by the generous financial support of the W.M. Keck Foundation. We wish to recognize and acknowledge the very significant cultural role and reverence that the summit of Mauna Kea has always had within the indigenous Hawaiian community. We are fortunate to have the opportunity to conduct observations from this mountain.

## REFERENCES

Abazajian K. N. et al., 2009, ApJS, 182, 543
Adelberger K. L., Steidel C. C., Shapley A. E., Hunt M. P., Erb D. K., Reddy N. A., Pettini M., 2004, ApJ, 607, 226
Arnouts S., Ilbert O., 2011, LePHARE: Photometric Analysis for Redshift Estimate, Astrophysics Source Code Library, record ascl:1108.009
Bian F. et al., 2010, ApJ, 725, 1877
Bian F., Kewley L. J., Dopita M. A., Juneau S., 2016, ApJ, 822, 62
Brinchmann J., Charlot S., White S. D. M., Tremonti C., Kauffmann G., Heckman T., Brinkmann J., 2004, MNRAS, 351, 1151
Brinchmann J., Pettini M., Charlot S., 2008, MNRAS, 385, 769
Cardelli J. A., Clayton G. C., Mathis J. S., 1989, ApJ, 345, 245
Cooper M. C., Newman J. A., Davis M., Finkbeiner D. P., Gerke B. F., 2012, spec2d: DEEP2 DEIMOS Spectral Pipeline, Astrophysics Source Code Library, record ascl:1203.003
Cowie L. L., Barger A. J., Songaila A., 2016, ApJ, 817, 57
Cullen F., Cirasuolo M., McLure R. J., Dunlop J. S., Bowler R. A. A., 2014, MNRAS, 440, 2300
Daddi E. et al., 2007, ApJ, 670, 156
Dickey C. M. et al., 2016, ApJ, 828, L11
Dickinson M., Papovich C., Ferguson H. C., Budavári T., 2003, ApJ, 587, 25
Dopita M. A., Sutherland R. S., 2003, Astrophysics of the Diffuse Universe. Springer-Verlag, Germany
Dopita M. A. et al., 2006a, ApJS, 167, 177
Dopita M. A. et al., 2006b, ApJ, 647, 244
Drory N., Salvato M., Gabasch A., Bender R., Hopp U., Feulner G., Pannella M., 2005, ApJ, 619, L131
Elbaz D. et al., 2011, A&A, 533, A119
Faber S. M. et al., 2003, in Iye M., Moorwood A. F. M., eds, Proc. SPIEConf. Ser Vol. 4841, Instrument Design and Performance for Optical/Infrared Ground-based Telescopes. SPIE, Bellingham, p. 1657, doi:10.1117/12.460346
Fischer C. F., Tachiev G., 2014 MCHF/MCDHF Collection, Version 2, Ref No. 10 & 20, National Institute of Standards and Technology. Available at: http://physics.nist.gov/mchf
Fontana A. et al., 2003, ApJ, 594, L9
Genzel R. et al., 2013, ApJ, 773, 68
Groves B. A., Heckman T. M., Kauffmann G., 2006, MNRAS, 371, 1559
Groves B., Dopita M. A., Sutherland R. S., Kewley L. J., Fischera J., Leitherer C., Brandl B., van Breugel W., 2008, ApJS, 176, 438
Haffner L. M. et al., 2009, Rev. Mod. Phys., 81, 969
Hainline K. N., Shapley A. E., Kornei K. A., Pettini M., Buckley-Geer E., Allam S. S., Tucker D. L., 2009a, ApJ, 701, 52
Hainline K. N., Shapley A. E., Kornei K. A., Pettini M., Buckley-Geer E., Allam S. S., Tucker D. L., 2009b, ApJ, 701, 52
Hao C.-N., Kennicutt R. C., Johnson B. D., Calzetti D., Dale D. A., Moustakas J., 2011, ApJ, 741, 124
Hayashi M. et al., 2015, PASJ, 67, 80
Holden B. P. et al., 2016, ApJ, 820, 73
Hopkins A. M., Beacom J. F., 2006, ApJ, 651, 142
Ilbert O. et al., 2013, A&A, 556, A55
Ilbert O. et al., 2015, A&A, 579, A2
Juneau S. et al., 2014, ApJ, 788, 88
Kashino D. et al., 2013, ApJ, 777, L8
Kashino D. et al., 2016, preprint (arXiv:1604.06802)
Kauffmann G. et al., 2003, MNRAS, 346, 1055
Kennicutt R. C., Jr1998, ApJ, 498, 541
Kennicutt R. C., Evans N. J., 2012, ARA&A, 50, 531
Kewley L. J., Dopita M. A., 2002, ApJS, 142, 35
Kewley L. J., Dopita M. A., Sutherland R. S., Heisler C. A., Trevena J., 2001, ApJ, 556, 121
Kewley L. J., Jansen R. A., Geller M. J., 2005, PASP, 117, 227

Downloaded from https://academic.oup.com/mnras/article/465/3/3220/2417054 by Library user on 15 March 2021

Kewley L. J., Dopita M. A., Leitherer C., Davé R., Yuan T., Allen M., Groves B., Sutherland R., 2013, ApJ, 774, 100
Kewley L. J., Zahid H. J., Geller M. J., Dopita M. A., Hwang H. S., Fabricant D., 2015, ApJ, 812, L20
Kobulnicky H. A., Kewley L. J., 2004, ApJ, 617, 240
Krumholz M. R., Matzner C. D., 2009, ApJ, 703, 1352
Laigle C. et al., 2016, ApJS, 224, 24
Levesque E. M., Kewley L. J., Larson K. L., 2010, AJ, 139, 712
Liu X., Shapley A. E., Coil A. L., Brinchmann J., Ma C.-P., 2008, ApJ, 678, 758
Madau P., Dickinson M., 2014, ARA&A, 52, 415
Masters D. et al., 2014, ApJ, 785, 153
McCracken H. J. et al., 2012, A&A, 544, A156
Mesa-Delgado A., Núñez-Díaz M., Esteban C., López-Martín L., García-Rojas J., 2011, MNRAS, 417, 420
Murphy E. J. et al., 2011, ApJ, 737, 67
Nakajima K., Ouchi M., 2014, MNRAS, 442, 900
Newman J. A. et al., 2013, ApJS, 208, 5
Newman S. F. et al., 2014, ApJ, 781, 21
Oke J. B., 1990, AJ, 99, 1621
Osterbrock D. E., Ferland G. J., 2006, Astrophysics of Gaseous Nebulae and Active Galactic Nuclei, 2nd edn. Univ. Sci. Books, Sausalito, CA
Rigby J. R., Wuyts E., Gladders M. D., Sharon K., Becker G. D., 2011, ApJ, 732, 59
Rudnick G. et al., 2003, ApJ, 599, 847
Sanders R. L. et al., 2016, ApJ, 816, 23
Scoville N. et al., 2007, ApJS, 172, 1
Shapley A. E. et al., 2015, ApJ, 801, 88
Shimakawa R. et al., 2015, MNRAS, 451, 1284
Shirazi M., Vegetti S., Nesvadba N., Allam S., Brinchmann J., Tucker D., 2014a, MNRAS, 440, 2201
Shirazi M., Brinchmann J., Rahmati A., 2014b, ApJ, 787, 120
Silverman J. D. et al., 2015, ApJS, 220, 12
Speagle J. S., Steinhardt C. L., Capak P. L., Silverman J. D., 2014, ApJS, 214, 15
Steidel C. C., Shapley A. E., Pettini M., Adelberger K. L., Erb D. K., Reddy N. A., Hunt M. P., 2004, ApJ, 604, 534
Steidel C. C. et al., 2014, ApJ, 795, 165
Tacconi L. J. et al., 2010, Nature, 463, 781
Tayal S. S., 2007, ApJS, 171, 331
Tayal S. S., Zatsarinny O., 2010, ApJS, 188, 32
Tremonti C. A. et al., 2004, ApJ, 613, 898
van der Wel A. et al., 2014, ApJ, 788, 28
Veilleux S., Osterbrock D. E., 1987, ApJS, 63, 295
York D. G. et al., 2000, AJ, 120, 1579
Zahid H. J., Dima G. I., Kewley L. J., Erb D. K., Davé R., 2012, ApJ, 757, 54
Zahid H. J. et al., 2014, ApJ, 792, 75

Downloaded from https://academic.oup.com/mnras/article/465/3/3220/2417054 by Library user on 15 March 2021

## APPENDIX A: DATA

**Table A1.** Summary of measurements for the $z \sim 1.5$ [O II]-H$\alpha$ detected sample.

| DEIMOS ID (1) | $\alpha$ (h) (2) | $\delta$ (deg) (3) | $z$ (mag) (4) | $z_{\rm spec}$ [O II] (5) | log M$_*$ (M$_\odot$) (6) | log SFR (M$_\odot$ yr$^{-1}$) (7) | [O II] (8) | [O II]$\lambda$3726 ($10^{-17}$ erg s$^{-1}$ cm$^{-2}$) (9) | [O II]$\lambda$3729 (10) | $n_{\rm e}$ (cm$^{-3}$) (11) |
|---|---|---|---|---|---|---|---|---|---|---|
| JK_28823 | 09:59:56.98 | +02:09:20.5 | 22.1 | 1.406 | 10.95 | 2.31 ± 0.22 | 2.99 ± 0.27 | 2.60 ± 0.20* | 0.40 ± 0.18* | – |
| D345075 | 09:59:37.82 | +02:14:23.2 | 23.4 | 1.427 | 10.66 | 1.11 ± 0.03 | 4.09 ± 0.30 | 1.65 ± 0.17* | 2.44 ± 0.23* | – |
| D464854 | 09:59:25.37 | +02:30:47.0 | 22.6 | 1.434 | 10.59 | 1.30 ± 0.05 | 6.21 ± 0.20 | 2.59 ± 0.12 | 3.62 ± 0.12 | $35^{+51}_{-35}$ |
| D409473 | 10:00:47.61 | +02:23:27.5 | 22.7 | 1.436 | 10.48 | 1.20 ± 0.05 | 3.36 ± 0.14 | 1.40 ± 0.08 | 1.96 ± 0.10 | $34^{+72}_{-34}$ |
| JK_38652 | 10:00:00.63 | +02:33:01.2 | 22.6 | 1.441 | 11.87 | 1.88 ± 0.24 | 2.14 ± 0.40 | 1.04 ± 0.80* | 1.10 ± 0.81* | – |
| D341519 | 10:00:29.08 | +02:13:55.2 | 23.6 | 1.444 | 10.29 | 0.75 ± 0.05 | 1.60 ± 0.08 | 0.65 ± 0.05 | 0.94 ± 0.05 | $9^{+75}_{-9}$ |
| D387090 | 09:59:19.37 | +02:20:14.0 | 22.6 | 1.452 | 10.68 | 1.39 ± 0.26 | 3.98 ± 0.20 | 1.82 ± 0.16 | 2.16 ± 0.18 | $218^{+216}_{-143}$ |
| D455626 | 09:59:55.34 | +02:29:33.5 | 22.9 | 1.452 | 10.77 | 1.45 ± 0.05 | 4.62 ± 0.27 | 1.75 ± 0.16 | 2.87 ± 0.18 | <10 |
| 1038215 | 09:59:56.32 | +02:10:03.0 | 23.3 | 1.457 | 9.64 | 1.13 ± 0.05 | 3.36 ± 0.22 | 1.46 ± 0.16 | 1.90 ± 0.14 | $113^{+171}_{-113}$ |
| D298530 | 09:59:42.10 | +02:08:06.3 | 22.2 | 1.470 | 11.54 | 1.71 ± 0.18 | 0.50 ± 0.13 | 0.25 ± 0.08 | 0.25 ± 0.09 | – |
| D451530 | 09:59:16.42 | +02:29:02.3 | 22.7 | 1.471 | 10.90 | 1.70 ± 0.05 | 9.05 ± 0.25 | 4.50 ± 0.18 | 4.55 ± 0.19 | $451^{+111}_{-92}$ |
| D344598 | 09:59:28.09 | +02:14:14.7 | 23.0 | 1.475 | 11.18 | 1.25 ± 0.05 | 1.91 ± 0.17 | 1.07 ± 0.14 | 0.85 ± 0.12 | $1018^{+1106}_{-473}$ |
| G174035 | 09:59:28.92 | +02:14:34.3 | 22.6 | 1.475 | 11.10 | 1.77 ± 0.05 | 3.12 ± 0.41 | 1.00 ± 0.76 | 2.12 ± 0.99 | – |
| G-9848 | 09:59:32.26 | +02:04:09.6 | 23.3 | 1.487 | 10.53 | 1.26 ± 0.11 | 1.38 ± 0.12 | 0.55 ± 0.07 | 0.83 ± 0.08 | <10 |
| G1190 | 09:59:47.15 | +02:06:27.5 | 22.6 | 1.489 | 11.09 | 1.53 ± 0.05 | 1.86 ± 0.16 | 0.62 ± 0.12 | 1.24 ± 0.12 | <10 |
| D394728 | 09:59:26.10 | +02:21:20.8 | 22.3 | 1.501 | 10.72 | 1.14 ± 0.07 | 11.12 ± 0.54 | 5.12 ± 0.53* | 6.00 ± 0.27* | – |
| G158505 | 09:59:14.52 | +02:11:33.9 | 23.1 | 1.504 | 10.86 | 1.64 ± 0.05 | 4.16 ± 0.85 | 1.93 ± 0.49* | 2.23 ± 0.67* | – |
| D319520 | 09:59:47.56 | +02:10:52.7 | 22.6 | 1.505 | 10.82 | 0.67 ± 0.13 | 6.00 ± 0.69 | 1.85 ± 3.15* | 4.15 ± 3.66* | – |
| 774526 | 10:00:20.96 | +02:04:07.4 | 23.9 | 1.506 | 10.38 | 0.70 ± 0.18 | 2.48 ± 0.19 | 1.20 ± 0.13 | 1.28 ± 0.11 | $365^{+245}_{-164}$ |
| G11751 | 09:59:40.07 | +02:08:31.7 | 23.2 | 1.507 | 10.28 | 1.28 ± 0.05 | 4.38 ± 0.32 | 1.73 ± 0.17 | 2.65 ± 0.22 | <10 |
| JK_16807 | 10:00:20.59 | +02:17:07.2 | 23.1 | 1.515 | 11.11 | 0.59 ± 0.16 | 2.34 ± 0.41 | 1.34 ± 0.41* | 1.00 ± 0.44* | – |
| 797988 | 09:59:50.77 | +02:04:49.9 | 22.8 | 1.519 | 11.16 | 1.26 ± 0.24 | 2.63 ± 0.53 | 1.57 ± 0.51* | 1.06 ± 0.21* | – |
| D490890 | 09:59:28.30 | +02:34:18.0 | 22.6 | 1.522 | 11.24 | 1.05 ± 0.07 | 1.57 ± 0.90 | 0.83 ± 0.77 | 0.74 ± 0.57 | – |
| G-14013 | 10:00:23.15 | +02:03:18.0 | 23.6 | 1.524 | 10.77 | 0.67 ± 0.05 | 2.59 ± 0.33 | 1.19 ± 0.26 | 1.41 ± 0.22 | – |
| D308265 | 09:59:27.44 | +02:09:27.7 | 23.1 | 1.524 | 10.57 | 1.17 ± 0.05 | 4.29 ± 0.17 | 1.73 ± 0.10 | 2.57 ± 0.11 | <10 |
| D325472 | 09:59:21.14 | +02:11:40.8 | 22.9 | 1.526 | 10.55 | 1.04 ± 0.18 | 7.93 ± 0.51 | 3.11 ± 0.21* | 4.81 ± 0.48* | – |
| D318267 | 09:59:18.30 | +02:10:44.8 | 23.3 | 1.526 | 10.20 | 1.15 ± 0.05 | 5.62 ± 0.54 | 2.20 ± 0.27* | 3.42 ± 0.57* | – |
| 1068560 | 09:59:34.50 | +02:07:46.6 | 24.0 | 1.540 | 10.06 | 0.85 ± 0.05 | 2.00 ± 1.10 | 2.00 ± 1.06* | 0.00 ± 0.43* | – |
| JK_41000 | 09:59:38.94 | +02:16:53.9 | 22.2 | 1.551 | 11.60 | 1.84 ± 0.05 | 4.15 ± 0.73 | 3.39 ± 1.22 | 0.76 ± 1.23 | – |
| D339009 | 09:59:15.01 | +02:13:33.8 | 23.2 | 1.550 | 9.96 | 1.16 ± 0.05 | 3.69 ± 0.38 | 1.95 ± 0.37* | 1.74 ± 0.20* | – |
| G26349 | 09:59:42.09 | +02:11:23.2 | 22.7 | 1.551 | 11.36 | 1.65 ± 0.05 | 5.86 ± 1.11 | 2.50 ± 2.99* | 3.36 ± 3.65* | – |
| D340558 | 09:59:38.19 | +02:13:40.7 | 23.1 | 1.580 | 10.40 | 1.03 ± 0.05 | 5.66 ± 0.59 | 1.88 ± 0.29* | 3.78 ± 0.52* | – |
| D307756 | 09:59:42.34 | +02:09:21.9 | 23.3 | 1.583 | 10.90 | 0.44 ± 0.05 | 6.82 ± 0.28 | 2.97 ± 0.23 | 3.86 ± 0.25 | $108^{+144}_{-104}$ |
| D416912 | 10:00:40.61 | +02:24:28.0 | 22.8 | 1.587 | 10.65 | 1.37 ± 0.20 | 5.44 ± 0.39 | 2.40 ± 0.26 | 3.04 ± 0.29 | $140^{+208}_{-135}$ |
| D332067 | 09:59:24.05 | +02:12:35.7 | 22.6 | 1.587 | 10.40 | 1.29 ± 0.14 | 12.23 ± 0.38 | 5.36 ± 0.25 | 6.87 ± 0.23 | $124^{+61}_{-52}$ |
| 220419_HJZ | 10:00:46.57 | +02:23:35.7 | 22.7 | 1.588 | 10.76 | 1.22 ± 0.05 | 5.10 ± 0.33 | 2.05 ± 0.23 | 3.05 ± 0.26 | <10 |
| D358016 | 09:59:22.34 | +02:16:10.7 | 23.3 | 1.587 | 10.48 | 1.17 ± 0.18 | 3.19 ± 0.26 | 1.39 ± 0.16 | 1.80 ± 0.18 | $113^{+180}_{-113}$ |
| G-8423 | 09:59:50.59 | +02:04:26.0 | 23.0 | 1.595 | 10.98 | 0.82 ± 0.05 | 1.46 ± 0.24 | 0.55 ± 0.17* | 0.91 ± 0.18* | – |
| D399476 | 09:59:29.23 | +02:22:01.0 | 23.5 | 1.617 | 10.47 | 1.05 ± 0.05 | 5.14 ± 0.56 | 0.80 ± 1.20 | 4.34 ± 1.30 | – |
| D352264 | 09:59:46.98 | +02:15:20.4 | 22.7 | 1.636 | 10.68 | 1.71 ± 0.05 | 5.04 ± 0.37 | 2.21 ± 0.24 | 2.83 ± 0.25 | $125^{+178}_{-121}$ |
| G-9661 | 09:59:49.26 | +02:04:09.7 | 23.3 | 1.638 | 10.90 | 0.52 ± 0.17 | 2.66 ± 0.38 | 1.39 ± 0.24 | 1.27 ± 0.23 | $641^{+847}_{-364}$ |
| G163773 | 10:00:22.60 | +02:12:34.2 | 23.3 | 1.641 | 10.47 | 1.20 ± 0.05 | 4.89 ± 0.81 | 1.28 ± 0.41* | 3.61 ± 0.75* | – |
| JK_16428 | 09:59:41.31 | +02:14:42.8 | 23.9 | 1.647 | 10.67 | 1.36 ± 0.17 | 8.43 ± 0.63 | 5.44 ± 6.47* | 2.99 ± 6.69* | – |
| G133455 | 09:59:43.00 | +02:06:36.7 | 23.5 | 1.652 | 9.81 | 1.32 ± 0.26 | 9.30 ± 0.60 | 4.32 ± 0.44 | 4.98 ± 0.43 | $250^{+225}_{-149}$ |
| 1032970 | 09:59:48.39 | +02:12:09.2 | 22.6 | 1.654 | 10.82 | 1.73 ± 0.05 | 9.66 ± 0.84* | 3.58 ± 0.46* | 6.08 ± 0.64* | – |
| JK_17606 | 10:00:36.31 | +02:21:17.5 | 23.0 | 1.654 | 10.54 | 2.02 ± 0.21 | 7.55 ± 0.94 | 3.09 ± 0.87* | 4.45 ± 0.83* | – |

Notes: (1) DEIMOS identifier assigned to target. (2) Right ascension (J2000) in units of hours, minutes and seconds. (3) Declination (J2000) in units of degrees, arcminutes and arcseconds. (4) Z(AB) magnitude. (5) Spectroscopic redshift determined from [O II]. (6) log(M$_*$/ M$_\odot$) from BC03 best-fitting template taken at the minimum $\chi^2$(Laigle et al. 2016). (7) log (SFR/ M$_\odot$ yr$^{-1}$) Calculated from H$\alpha$ based on Cardelli et al. (1989) treatment of extinction. (8) Total [O II]$\lambda\lambda$3726,3729 flux. (9) [O II]$\lambda$3726 flux. (10) [O II]$\lambda$3726 flux. (11) Electron density estimated from [O II]$\lambda$3726/$\lambda$3729.

Downloaded from https://academic.oup.com/mnras/article/465/3/3220/2417054 by Library user on 15 March 2021

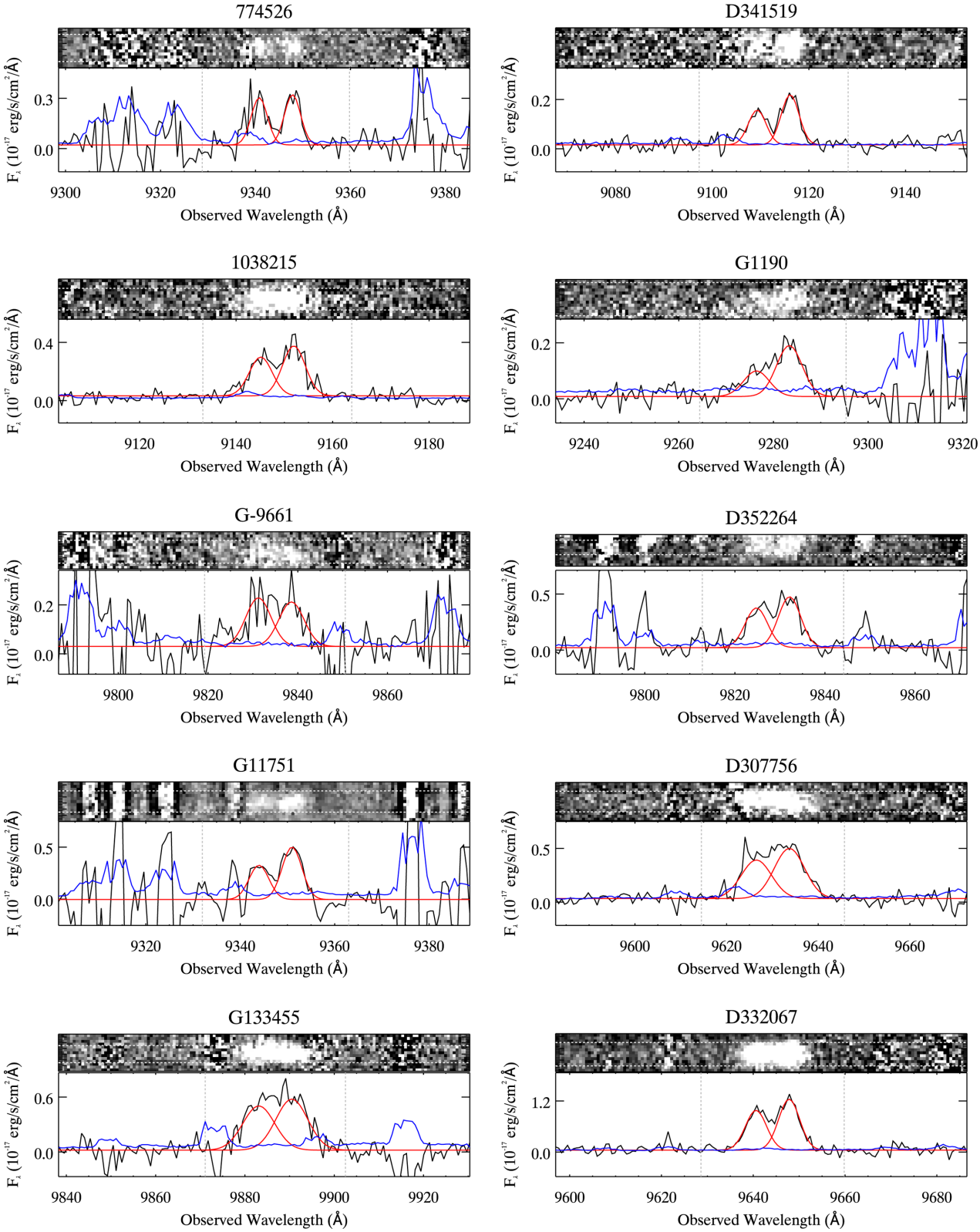


**Figure A1.** Wavelength and flux calibrated spectra for our [O II]-H$\alpha$ detected electron density sample. Corresponding 2D (grey-scale) and 1D (black line) DEIMOS spectra are shown in the top and bottom panels, respectively. Continuum and [O II] emission-line fits are shown alongside the 1D spectra in red. 1D 'noise' spectra (used to weight the fits) are indicated in blue. The effective apertures are marked for the 2D spectra (horizontal white dashed lines). The wavelength regions considered for fitting the [O II] doublets are bounded by vertical grey dashed lines.

Downloaded from https://academic.oup.com/mnras/article/465/3/3220/2417054 by Library user on 15 March 2021

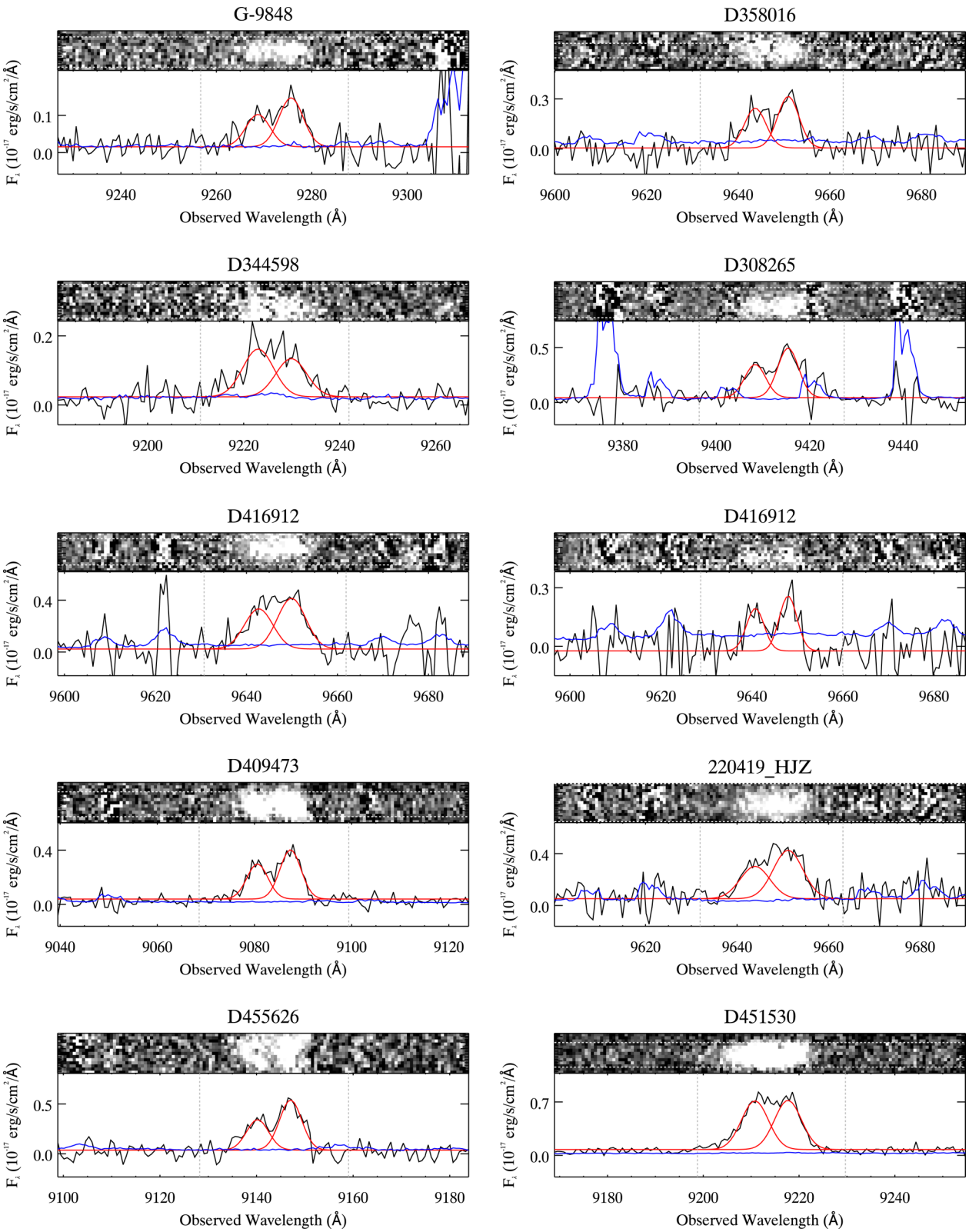


**Figure A1** – *continued*

Downloaded from https://academic.oup.com/mnras/article/465/3/3220/2417054 by Library user on 15 March 2021

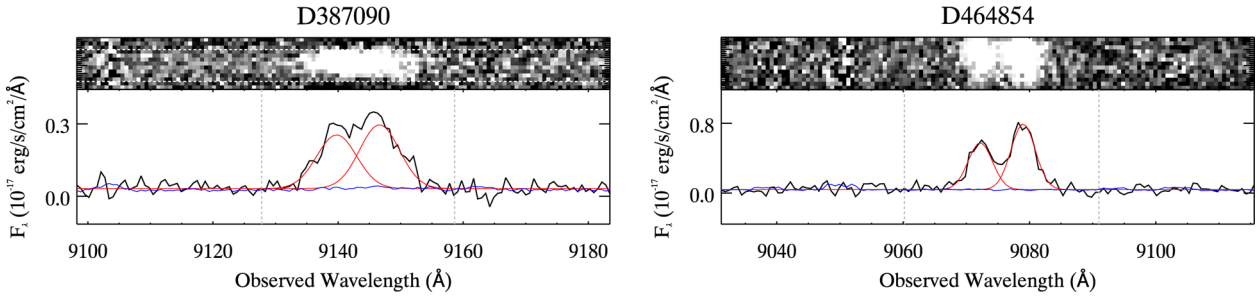


**Figure A1** – *continued*

This paper has been typeset from a TEX/LATEX file prepared by the author.

Downloaded from https://academic.oup.com/mnras/article/465/3/3220/2417054 by Library user on 15 March 2021